

Assessment of future changes in Southeast Asian precipitation using the NASA Earth Exchange Global Daily Downscaled Projections data set

Mandapaka, Pradeep V.; Lo, Edmond Yat Man

2018

Mandapaka, P. V., & Lo, E. Y. M. (2018). Assessment of future changes in Southeast Asian precipitation using the NASA Earth Exchange Global Daily Downscaled Projections data set. *International Journal of Climatology*, 38(14), 5231-5244. doi:10.1002/joc.5724

<https://hdl.handle.net/10356/137177>

<https://doi.org/10.1002/joc.5724>

© 2018 Royal Meteorological Society. All rights reserved. This paper was published in *International Journal of Climatology* and is made available with permission of Royal Meteorological Society.

Downloaded on 09 Apr 2024 10:17:49 SGT

1 Assessment of future changes in Southeast Asian Precipitation
2 using the NASA Earth Exchange global daily downscaled
3 projections (NEX-GDDP) dataset

4 Pradeep V. Mandapaka*¹ and Edmond Y.M. Lo^{1,2}

5 ¹Institute of Catastrophe Risk Management

6 ²School of Civil and Environmental Engineering

7 Nanyang Technological University, 50 Nanyang Avenue, Singapore 639798

8 May 16, 2018

*Corresponding author email: pradeepmv@ntu.edu.sg, Tel.: +65 65921870

Abstract

Extreme precipitation and associated flooding cause severe damage to society and the environment. Future climate projections suggest an intensification of precipitation extremes in many regions. However, there is an increasing need for climate change impact assessment at higher spatial resolution, particularly for regions with complex geography such as Southeast Asia (SEA). In this study, we analysed the NASA Earth Exchange 0.25° resolution daily precipitation projections from an ensemble of 20 climate models under two emission scenarios RCP4.5 and RCP8.5. The variability in future precipitation projections is analysed and quantified for six geographical subregions, two climatological regions (wet and dry), and the low elevation coastal zones in SEA. Various aspects of precipitation structure are studied using indices that characterize precipitation amount, number of heavy precipitation days, extreme precipitation amount, and maximum daily precipitation at annual and seasonal scales. The results show substantial increases in mean and extreme precipitation in many parts of SEA by the end of the 21st century under both emission scenarios, thus increasing the region's vulnerability to precipitation driven hazards. The projected centennial increase in total annual precipitation relative to the baseline period of 1970-1999 when averaged over all land grid cells is about 15% under RCP8.5 scenario, with larger values (~20%) over mainland SEA and Philippines and smaller values (~6%) in Java island. The projected changes in extreme precipitation are stronger compared to the total annual precipitation under both emission scenarios. The New Guinea and Java regions show the largest and smallest increases in annual maximum daily precipitation, with ensemble mean values of 30% and 17%, respectively under RCP8.5 scenario. The results also reveal large intermodel spread in projected changes, particularly during boreal winter and summer months.

Keywords: Precipitation extremes; Climate change; Maritime Continent; Spatial analysis; NEX-GDDP

1 Introduction

Southeast Asia (SEA, Figure 1a) has more than 20000 islands, complex topography, and a population of ~633 million that is projected to reach 792 million by the year 2050 (UNPD, 2015). The region is home to densely populated megacities including Bangkok, Jakarta, and Manila. A significant fraction of the region’s population lives in deltas or coastal areas, and is exposed to riverine and coastal flooding (e.g., Jongman et al., 2012; Arnell and Gosling, 2016). For example, the 2011 Thailand floods lasted for 158 days and caused a number of fatalities along with heavy economic losses (e.g., World Bank, 2012; Haraguchi and Lall, 2015; Promchote et al., 2016). Similarly, the city of Jakarta, which has a population of 10 million, experienced severe flooding in recent years (e.g. in 2007, 2013, and 2014) with economic losses in the order of hundreds of millions of dollars (e.g., Budiyo et al., 2015).

A warmer climate implies an increase in atmospheric moisture at a Clausius-Clapeyron rate of around 7% K^{-1} and amplification of the precipitation structure (e.g., Held and Soden, 2006; Pall et al., 2007; O’Gorman and Schneider, 2009). A number of observational and model based studies reported significant changes in precipitation characteristics, particularly in extremes (e.g., Fischer et al., 2013; Toreti et al., 2013; Westra et al., 2013; Liu and Allan, 2013; Chadwick et al., 2016; Donat et al., 2016; Pfahl et al., 2017). Intensification of future precipitation extremes can have severe consequences on society and the environment in the form of increased frequency and intensity of droughts, floods, and landslides (e.g., Field et al., 2012; IPCC, 2014). Increasing population and rapid urbanization further exacerbate the vulnerability of a region to the changing climate (e.g., Winsemius et al., 2016). Moreover, agricultural area covers about 30% of SEA’s land area (Food and Agricultural Organization, 2017), and is an important contributor to the region’s economy (e.g., 27% of Cambodia’s GDP; World Bank, 2017). As a substantial part of agriculture in SEA is rainfed (e.g., Johnston et al., 2012), any future changes in precipitation structure may have an impact on agricultural productivity (e.g., Masutomi et al., 2009; Chun et al., 2016) and the economy of the region. Therefore, understanding the nature of changes in precipitation structure is of major importance for developing climate resilient water management programs in the region.

Much information regarding the projected changes in SEA precipitation is embedded in global

scale studies carried out using global climate models (GCM) (e.g., Fischer et al., 2013; Kharin et al., 2013; Sillmann et al., 2013; Chadwick et al., 2016). The complex geography (e.g., land-sea structure and long coastlines) of SEA necessitates quantification of changes in precipitation at a resolution higher than a typical GCM resolution of 2.5° . Moreover, there is a strong demand from policy makers for local to regional scale assessment of changes in future precipitation patterns in SEA for planning new infrastructure to mitigate the impacts on society and environment. A small number of studies, which assessed future changes in SEA precipitation at higher resolution have done so for specific river basins or using a specific climate model (e.g., Chotamonsak et al., 2011; Lacombe et al., 2012; Tan et al., 2017). The aim of this study is to further our understanding of the impacts of changing climate on SEA precipitation at a resolution finer than the GCMs. For this purpose, we employed the NASA Earth Exchange Global Daily Downscaled Projections (NEX-GDDP; Thrasher et al., 2012) and assessed the changes in precipitation characteristics at a spatial resolution of 0.25° . We conducted the analysis by focusing on different subregions (geographical, climatological, and elevation based) within SEA. Section 2 provides a description of the NEX-GDDP dataset. Section 3 describes the list of indices employed, subregions, and the methods used to quantify changes. The results are discussed in section 4, followed by concluding remarks in section 5.

2 NEX-GDDP dataset

The historical and future precipitation for this study is obtained from the NEX-GDDP dataset available at <https://cds.nccs.nasa.gov/nex-gddp/>. The historical record of the data spans from 1950 to 2005 and projections are available from 2006 to 2099 for representative concentration pathways (RCP) 4.5 and 8.5. The RCP4.5 represents an intermediate emissions scenario with stabilization of radiative forcing to 4.5 W m^{-2} by the year 2100, whereas RCP8.5 is a high emissions scenario with increasing greenhouse gases throughout the twenty-first century leading to a radiative forcing of 8.5 W m^{-2} by 2100 (e.g., Van Vuuren et al., 2011; Taylor et al., 2012).

The NEX-GDDP dataset is available for entire globe at a spatial resolution of 0.25° and at a daily scale. The finer spatial resolution NEX-GDDP dataset was generated from coarse resolution GCMs of Coupled Model Intercomparison Project Phase 5 (CMIP5) using bias correction spatial

disaggregation (BCSD; Wood et al., 2004; Thrasher et al., 2012) method. The BCSD approach as implemented for NEX-GDDP data, corrects the bias in GCMs at a coarser resolution based on quantile mapping and using the gridded observations from the Global Meteorological Forcing Dataset (Sheffield et al., 2006) for the period of 1950-2005. The bias corrected GCMs are then spatially disaggregated using scaling factors and bilinear interpolation to a finer resolution of 0.25° . Further details regarding the application of BCSD method and the generation of NEX-GDDP dataset can be found in Thrasher et al. (2012) and Thrasher and Nemani (2015). The NEX-GDDP data has been used in a number of studies to assess changes in precipitation and temperature at regional scales (e.g., Ahmadalipour et al., 2017; Bao and Wen, 2017; Chen et al., 2017; Daksiya et al., 2017; Maurer et al., 2017). For this study we employed historical and future precipitation from an ensemble of 20 GCMs in NEX-GDDP dataset (see Table S1 in supplementary material for details) for the region extending from 90°E - 150°E and 10°S - 20°N .

3 Methods

3.1 Indices employed

We used four indices in this study: i) precipitation total (PRCPTOT), ii) number of days with precipitation $\geq 10 \text{ mm day}^{-1}$ (R10), iii) total precipitation from days $\geq 95\text{th}$ percentile of daily precipitation (R95P), and iv) maximum daily precipitation (RX1DAY). The indices and their units are listed in Table 1. These indices were selected to focus on total precipitation during a period as well as different aspects of extremes. The index R10, which is defined based on a fixed threshold of 10 mm day^{-1} characterizes the frequency of “heavy” precipitation days (e.g., Zhang et al., 2011). However, it may not quantify the extreme precipitation days for all regions because of spatially varying precipitation probability distributions. On the other hand, R95P being based on a percentile threshold, takes into account the regional variability in precipitation climatology, and characterizes the specific tail part (exceedance probability of 5%) of precipitation distribution (Table 1). Specifically, R95P quantifies the amount of precipitation resulting from the top 5% (i.e. very wet) rainfall days in each year. It is noted that a threshold of 1 mm day^{-1} was used to define rainy days. The light precipitation is not considered in this study as it is prone to large uncertainties in climate model simulations. In addition, we normalized

the indices at each grid cell with the corresponding climatological value obtained for the baseline period (1970-1999). The normalization was performed to minimize the effect of large spatial variations on regional averages. It is also noted that the normalization was done for each model separately using model-specific baseline climatology.

3.2 Extreme value analysis

As infrastructure design and planning is commonly based on T -year return level (the value that is exceeded with a probability of $1/T$), it is also of interest to assess changes in precipitation extremes of specific return period T . Unlike the indices described in section 3.1, which are derived from empirical frequency distributions of wet day precipitation amounts, the T -year return levels of precipitation extremes are obtained using extreme value theory (EVT) and the block (e.g., annual, seasonal) maxima approach. Another approach to study extremes under the EVT framework is the peaks-over-threshold method (POT), where precipitation values above a particular threshold are analyzed. We used the block maxima (RX1DAY values) approach instead of POT method as the assumption that the values are independent and identically distributed (i.i.d) is better satisfied with the former (e.g., Kao and Ganguly, 2011). The RX1DAY values were then fitted with a Generalized Extreme Value (GEV) distribution, which was selected because it is the asymptotic distribution for block maxima (e.g., Coles, 2001; Castillo et al., 2005). The block maxima approach in conjunction with GEV distribution was used in many previous studies on hydrologic extremes (e.g., Kharin et al., 2007; Kao and Ganguly, 2011; Villarini et al., 2011; Kharin et al., 2013). The cumulative distribution function of a GEV distribution is given by

$$F(x|\mu, \sigma, k) = \begin{cases} \exp\left(-\left[1 + \frac{k(x-\mu)}{\sigma}\right]^{-1/k}\right), & \text{for } 1 + \frac{k(x-\mu)}{\sigma} > 0, k \neq 0 \\ \exp\left(-\left[\frac{(x-\mu)}{\sigma}\right]\right), & \text{for } -\infty < x < \infty, k = 0 \end{cases} \quad (1)$$

where $\mu \in (-\infty, \infty)$, $\sigma > 0$, and $k \in (-\infty, \infty)$ are location, scale and shape parameters, respectively. When $k = 0$, the distribution is extreme value type I or Gumbel distribution, whereas $k > 0$ (unbounded above) and $k < 0$ (unbounded below) results in Fréchet and Weibull distributions, respectively.

3.3 Trend and time slice analysis

We assessed changes in precipitation structure using two approaches. The first method consists of evaluating the significance of trends in precipitation indices using the Mann-Kendall (MK) nonparametric test (e.g., Kendall, 1975; McCuen, 2002) at a significance level of 5%. The magnitude of the trend was then obtained using Sen's nonparametric regression, which is more robust to the presence of outliers (e.g., Sen, 1968). The slope of the regression line (or Sen's slope) was estimated as the median of pairwise slopes between elements of the time series (e.g., Hess et al., 2001; Yue et al., 2002). Both MK test and Sen's regression are extensively used in earth sciences for assessing trends (e.g., Gan, 1998; Yue et al., 2002; Alexander and Arblaster, 2009; Westra et al., 2013; Mandapaka et al., 2016). More details about the MK test and Sen's regression can be found in Hess et al. (2001), McCuen (2002), or Yue et al. (2002). It is noted that Sen's slope is an estimate of the linear trend in time series. Alternatively, we also quantified the changes in future precipitation by computing average indices for a 30-year future time slice 2070-2099. The time-slice analysis provides a straightforward approach to assess the long-term changes relative to the baseline period. The changes are quantified for each index and for each grid cell, and their spatial variability is analyzed.

3.4 Delineation of regional masks

In order to compare changes in precipitation across different regions, some level of spatial aggregation is required. For this purpose, the land grid cells in the study area were grouped into nine subregions, out of which six were delineated based on geography (Figure 1(b)), two masks are based on precipitation climatology (Figure 1(c)), and one mask based on topography and proximity to the sea. Table 2 lists the regional masks and their fractional land coverage. Among the six geographical masks, continental southeast Asia (CSEA) is the largest and covers 27.3% of the land area in the study domain. The mask SRMP includes Sumatra, Malay Peninsula and Singapore and covers 14.9% of the land area. The islands of Borneo and Sulawesi are analyzed together in this study and the region is hereafter referred to as BORS. The Java and nearby smaller islands are part of the mask JAVA, whereas Philippines archipelago forms the mask PHIL. The mask JAVA is the smallest among the six geographical masks, with a coverage of 6.5% of the land area.

The purpose of the two climatological masks is to compare future precipitation characteristics in dry and wet areas of the study region. For each model, we classified grid cells within the bottom and top quartiles of base period PRCPTOT as dry and wet cells, respectively. It is noted that the classification is carried out only for land grid cells based on land-only PRCPTOT. Accordingly, the dry and wet masks are referred to as L-dry and L-wet, respectively. When the dry and wet regions are identified based on both land and sea PRCPTOT, most of the land grid cells are classified as wet because of the large contrast in land versus sea PRCPTOT. Figure 1(c) shows the extracted L-dry and L-wet regions, with the color scale indicating the number of models that classify a particular cell as dry or wet. There is a good inter-model agreement in the spatial distribution of dry and wet grid cells, with $\sim 82\%$ of grid cells having a model count of at least 17 out of 20. The wet regions are mainly present in Borneo and New Guinea, with other cells distributed along the western coasts of Sumatra and Myanmar, and eastern Philippines. The location of wet regions are mainly determined by the interaction of the monsoon winds with the terrain (Figures 1a and 1c) (e.g., Chang et al., 2005; Mandapaka et al., 2017). The dry grid cells are mainly concentrated in CSEA, with others present in Java and nearby islands.

The ninth regional mask used in the study focuses on low elevation coastal zones (LECZ), which are delineated using the U.S. National Geophysical Data Center’s ETOPO1 dataset. The ETOPO1 one arc-min resolution elevation data are regridded to 0.25° resolution (i.e. the resolution of the NEX-GDDP dataset) and the coastal grid cells with elevation below 25 m are categorized as LECZ region. The LECZ grid cells occupy about 5.5% of the study area.

4 Results and discussion

The indices described in section 3.1 are obtained for each year and grid cell, and normalized with corresponding baseline period climatological indices. The normalized indices are then averaged over all nine regional masks. Figure 2 shows the temporal evolution of normalized indices for the six geographical subdomains in terms of ensemble mean ± 1 standard deviation. The PRCPTOT time series for RCP4.5 and RCP8.5 follow a similar pattern for much of the study period. However, the extreme precipitation indices R95P and RX1DAY tend to diverge after 2050. The results indicate considerable change in indices by the end of twenty-first century for

all six regions. The regions L-dry, L-wet, and LECZ also show substantial changes by the end of twenty-first century (Figure 3). In subsequent sections, we describe the spatial distribution of projected changes and quantify their regional variation.

4.1 Spatial patterns in ensemble mean response

We evaluated the time series of ensemble mean at each grid cell for the presence of monotonic trends using the MK test with a significance level of 5%. The trends were then quantified using Sen’s regression. It is noted that the trend analysis was performed on the time series from 2006-2099, i.e. on the model projections. Figure 4 shows the spatial distribution of trends in ensemble mean PRCPTOT and RX1DAY for RCP4.5 and RCP8.5 scenarios. The stippled pattern in Figure 4 denotes grid cells with trends that are statistically significant at 5%. The indices exhibit significant upward trend, particularly in land grid cells under both emission scenarios. However, the trends are weaker south of the equator, with the exception of NGUI. PRCPTOT can increase at a rate of 3-3.5% decade⁻¹ in northern parts of CSEA and PHIL, and 0.5-1% decade⁻¹ in JAVA under RCP8.5 scenario. The trends in RX1DAY exceed 4% decade⁻¹ for Central Borneo, northern parts of CSEA and in many parts of NGUI. Some grid cells in the Indian Ocean region southwest of Sumatra and Java show a decline in PRCPTOT under both scenarios, but RX1DAY is projected to increase in these pixels. From RCP4.5 to RCP8.5, the magnitude of trends rise sharply for the RX1DAY (Figure 4c to 4d) compared to the PRCPTOT (Figure 4a to 4b), indicating that the precipitation extremes are more sensitive to changes in emission scenarios.

It is noted that the magnitude of trends in Figure 4 were obtained assuming linearity. Therefore, we also quantified the changes in indices using time-slice analysis, wherein the average index during the 2070-2099 period at each grid cell is compared with that of the baseline period 1970-1999. Figure 5 shows the spatial distribution of centennial changes in ensemble mean PRCPTOT and RX1DAY for the two RCP scenarios. The spatial patterns in Figure 5 are consistent with those of trend analysis in Figure 4. With the exception of the Indian Ocean region southwest of Sumatra and Java, the study domain experiences wetter conditions by the end of the 21st century relative to the 1970-1999 baseline period under both RCP scenarios. For a majority of grid cells, particularly for RX1DAY, at least 15 models agree on the sign of change of ensemble

mean (see stippled pattern in Figure 5). The average projected increase in PRCPTOT by the end of 21st century can be as high as 29% under RCP8.5 scenario in northern parts of CSEA, and in PHIL. The projected changes in RX1DAY are more pronounced, with values exceeding 40% in Central Borneo, parts of NGUI, Thailand and Myanmar.

4.2 Regional averages of projected changes

Figure 6 displays centennial changes in four indices averaged over nine different land masks. The vertical bars represent the intermodel spread in the form of ensemble mean ± 1 standard deviation. The average projected increases in PRCPTOT across all land regions (dashed lines in Figure 6) are 9% and 15% under RCP4.5 and RCP8.5, respectively. The ensemble mean increase of 15% in PRCPTOT obtained here under RCP8.5 lies towards the higher end of the interquartile range of 5-15% shown for SEA in Sillmann et al. (2013) based on CMIP5 GCMs at their original resolution. Larger values in this study could be partly due to finer resolution projections used. Figure 6 also reveals large intermodel spread and significant regional variability in the projected changes in all four indices. Among the six geographical masks, CSEA and PHIL show larger changes in PRCPTOT, with values of 19% ($\pm 15\%$) and 20% ($\pm 18\%$), respectively under RCP8.5. The regions SRMP and BORS show an ensemble mean PRCPTOT increase of 9% and 11%, respectively, whereas JAVA shows weaker changes with an ensemble mean value of 6% under RCP8.5.

The ensemble mean projected increases in R10 when averaged over all land cells are 9% and 13% under RCP4.5 and RCP8.5, respectively (Figure 6). The largest increases in R10 are projected for PHIL with values of 19% ($\pm 18\%$) followed by NGUI with values of 15% ($\pm 15\%$) under RCP8.5. The projected changes in R95P follow a pattern that is similar to PRCPTOT and R10, i.e., larger changes for CSEA, PHIL and NGUI, and weaker response for JAVA. On average, the R95P across land cells is projected to increase by 13% and 21% under RCP4.5 and RCP8.5, respectively. The index RX1DAY shows a more pronounced increase compared to other indices. The ensemble mean projected increase in RX1DAY averaged across all land cells is 15% and 26% under RCP4.5 and RCP8.5, respectively. The projected increase in RX1DAY is the largest for NGUI with a value of 30% ($\pm 20\%$) followed by CSEA with a value of 28% ($\pm 12\%$) under RCP8.5 scenario.

The projections reveal an increase in PRCPTOT in both L-Dry and L-Wet regions with centennial changes of 18% ($\pm 14\%$) for the former and 15% ($\pm 12\%$) for the latter under RCP8.5. Similarly, RX1DAY in L-Dry and L-wet regions is projected to increase by 26% ($\pm 12\%$) and 29% ($\pm 17\%$), respectively under RCP8.5. In general, the results are consistent with Donat et al. (2016), which showed similar projected changes in RX1DAY over global dry and wet land regions. In LECZ, the PRCPTOT and RX1DAY are projected to increase by 11% and 22% on average, respectively under RCP8.5. The above pattern is similar for RCP4.5 scenario although with smaller changes. Overall comparison of results for RCP4.5 and RCP8.5 shows that the precipitation extremes are more sensitive to the changes in emissions than PRCPTOT and R10. For example, average projected increase in PRCPTOT over land grid cells changes from 9% for RCP4.5 to 15% for RCP8.5, whereas the corresponding increase in RX1DAY is 15% for RCP4.5 and 26% for RCP8.5. This general pattern is noticed at subregional scales as well (e.g. CSEA, SRMP in top and bottom panels of Figure 6).

The shaded boxes enveloping the vertical bars in Figure 6 represent the standard deviation computed by pooling in all the grid-level projected changes (without averaging) for each region. Therefore, the shading indicates both intermodel spread and spatial variability within a region, and is always larger than the one shown by vertical bars. Expectedly, the spatial variability is minimal for smaller regions JAVA and PHIL. The CSEA region, which is the largest among the geographical masks shows considerable spatial variability in projected changes, in the form of large spread of the shaded box compared to the vertical bar. The masks L-Dry, L-Wet and LECZ also show high spatial variability because the corresponding grid cells are spread out over different regions (see Figure 1c).

To this point, we analyzed precipitation extremes using indices R95P and RX1DAY. To quantify changes in extremes of specific return periods, we used EVT framework described in section 3.2. We pooled all RX1DAY values within each 3×3 box surrounding a grid cell and the 30-year baseline period of 1970-1999 (assuming stationarity within this period), resulting in 270 values for each grid cell. The choice of a 3×3 box instead of single cell was to minimize the effect of sampling (270 vs 30 values) in the fitting process. The pooled RX1DAY values at each grid cell were then fitted with a GEV distribution (equation 1) using the maximum likelihood method (e.g., Coles, 2001; Kottegoda and Rosso, 2008). The process was then repeated for the

future time period 2070-2099 for RCP4.5 and RCP8.5 scenarios. The goodness of fit of the GEV distribution for baseline and future periods was evaluated using Kolmogorov-Smirnov (KS) test at a significance level of 5%. As parameters of the GEV distribution were obtained from the data, we followed Monte Carlo approach (e.g., Kottegoda and Rosso, 2008; Villarini et al., 2011) to obtain critical values for the KS test. For the grid cells which passed the KS test, the GEV distribution parameters were used to obtain precipitation return levels with an exceedance probability of 0.05 ($T = 20$ years), 0.02 ($T = 50$ years), and 0.01 ($T = 100$ years).

Figure 7 shows the changes in 50-year return values for the 2070-2099 period relative to the 1970-1999 period. On average, the projected increase in 50-year return levels across land grids is 14% (22%) for RCP4.5 (RCP8.5) scenario. BORS and NGUI have larger changes in return levels compared to other regions under both scenarios. JAVA and PHIL regions have smaller projected changes in return levels compared to other regions. The wet regions experience slightly larger changes in 50-year return levels compared to dry regions for both scenarios. The projected changes in return levels were found to be larger for longer return periods. For example, the ensemble mean projected increase in 50-year and 100-year return levels over CSEA region under RCP8.5 scenario are 23% and 39%, respectively (Figures 7 and S2). Overall, from Figures 6 and 7, it is concluded that the extremes are projected to increase at a faster rate compared to the total precipitation.

4.3 Seasonal analysis

Many regions in the study domain experience significant annual cycle in precipitation (e.g., Chang et al., 2005). The interactions between seasonal winds and the underlying terrain play a major role in determining the precipitation hotspots (e.g., Chang et al., 2005; Mandapaka et al., 2017). We repeated the analysis at seasonal scale by computing the indices separately for March-May (MAM), June-August (JJA), September-November (SON), and December-February (DJF) months. Figure 8 displays the projected changes in regionally averaged indices for four seasons for the time period 2070-2099 relative to the baseline period 1970-1999. The average projected increases in boreal spring PRCPTOT across land regions are about 11% and 13% under RCP4.5 and RCP8.5 scenarios, respectively. The highest (lowest) ensemble mean increase in boreal spring PRCPTOT is projected for PHIL (CSEA) region. Similarly, the projected changes in R10 and

317 R95P are larger for PHIL and weaker for CSEA under both emission scenarios. However, both
 318 PHIL and CSEA regions have large intermodel spread in all three indices (PRCPTOT, R10 and
 319 R95P) during boreal spring. For example, PHIL has a projected increase in PRCPTOT of 23%
 320 ($\pm 32\%$) in boreal spring compared to the annual value of 20% ($\pm 18\%$) under RCP8.5 scenario.
 321 The large intermodel spread in PHIL and CSEA is mainly because of the drier climatology in
 322 these regions during boreal spring (Figure S1 in supplementary material), with the mean daily
 323 precipitation in many grid cells $< 3.5 \text{ mm day}^{-1}$ (e.g., Mandapaka et al., 2017). The same effect
 324 is also observed in the form of larger intermodel spread for L-Dry grid cells in boreal spring. The
 325 average projected increase in MAM RX1DAY across all land areas is 21% under RCP8.5, with
 326 the largest average increase of 28% in NGUI.

327 In JJA months, the average projected increase in PRCPTOT across land regions is about
 328 15% under RCP8.5, with near-zero values for JAVA and highest values for PHIL. However, the
 329 intermodel model spread for JAVA is large compared to other regions. During JJA months,
 330 JAVA region is dry (Figure S1), with the mean daily precipitation $< 2 \text{ mm day}^{-1}$ in a majority
 331 of its grid cells (e.g., Mandapaka et al., 2017). Furthermore, many grid cells in JAVA have zero
 332 JJA seasonal precipitation during the baseline period, which cannot be included in the analysis
 333 because all the future changes are computed relative to the baseline period. The remaining few
 334 grid cells with non-zero seasonal precipitation result in large intermodel spread for JAVA. Other
 335 indices also show a similar pattern for JAVA during JJA months. On average, the JJA R95P
 336 and RX1DAY for land regions are projected to increase by 22% and 24%, respectively under
 337 RCP8.5, with larger values for PHIL and NGUI.

338 For SON PRCPTOT, the largest ensemble mean increase of 26% is projected in CSEA fol-
 339 lowed by an increase of 23% for NGUI under RCP8.5. On average, the SON PRCPTOT is
 340 declining in JAVA by 6% but a large intermodel standard deviation of 29% is observed. The
 341 results for SON R10 and R95P are similar to those of PRCPTOT. Among the four indices, the
 342 intermodel agreement is higher for projected changes in RX1DAY, with values of 31% ($\pm 17\%$)
 343 in CSEA, and 29% ($\pm 23\%$) in NGUI under RCP8.5. For DJF months, the average projected
 344 changes in PRCPTOT for land grid cells is 12% under RCP8.5 scenario, with the largest value of
 345 25% ($\pm 38\%$) for PHIL. Very similar to the results for JAVA during JJA months, large intermodel
 346 spread (35-40%) in projected PRCPTOT for CSEA, PHIL and L-Dry regions is due to very low

seasonal precipitation in these regions (Figure S1). The pattern is similar for other indices during DJF months. The DJF RX1DAY is projected to increase by 19% over land regions under RCP8.5 with the largest values of 24% ($\pm 18\%$) in NGUI.

When averaged over all land grid cells in the study domain, the annual cycle (dashed lines in Figure 8) in projected changes is negligible. For example, PRCPTOT over land areas is projected to increase on average by 13%, 15%, 16% and 12% for MAM, JJA, SON and DJF months, respectively compared to the annual value of 15% under RCP8.5. Similarly, the ensemble mean increase in RX1DAY when averaged across land grid cells ranges from 19% in DJF to 24% in JJA months under RCP8.5. However, individual regional masks CSEA and PHIL display considerable annual cycle with ensemble mean projected changes in PRCPTOT ranging from 6-26% and 12-27%, respectively.

5 Summary and concluding remarks

This paper presented regional scale assessment of the response of SEA precipitation to the warming climate using the recently released statistically downscaled climate model projections from the NASA Earth Exchange. The impacts of climate change on regional precipitation patterns was assessed at a spatial resolution of 0.25° . Different aspects of precipitation structure were analyzed using four indices (PRCPTOT, R10, R95P and RX1DAY), which characterize precipitation amount, frequency and extremes. The projected changes in these four indices were quantified using trend analysis and time-slice comparison.

Results revealed significant positive trends in the ensemble mean projections of all four indices in a majority of the study domain. The trends in PRCPTOT were stronger in northern parts of CSEA, and weaker in JAVA region, with the values of 3-3.5% and 0.5-1% decade⁻¹, respectively. The trends in precipitation extremes were found to be stronger than those in annual precipitation total under both emission scenarios. The results from the time-slice comparison were consistent with those of trend analysis, with stronger projected increases in the northern parts of CSEA and weaker changes south of the equator.

The regional variability and intermodel spread were studied by grouping grid cells into nine

subregions: six geographical, two climatological (dry and wet), and one mask based on topography and proximity to the coast. All six geographic subregions showed substantial increase in annual total precipitation and extremes by the late 21st century. Relative to the baseline period of 1970-1999, PRCPTOT in land cells is projected to increase by 9% and 15% under RCP4.5 and RCP8.5, respectively, with larger changes in CSEA, PHIL and NGUI and weaker response in JAVA. The average projected changes in other three indices (R10, R95P and RX1DAY) followed a similar regional pattern as PRCPTOT, although with larger magnitudes. The index RX1DAY shows the most pronounced increase compared to other indices, with values of 15% and 26% for land grid cells under RCP4.5 and RCP8.5, respectively. Furthermore, the changes in projections from RCP4.5 to RCP8.5 were found to be stronger for precipitation extremes (R95P and RX1DAY) compared to the precipitation total (PRCPTOT) and frequency (R10) implying that extremes are more sensitive to global warming.

Considerable increase in all four indices is projected for both L-Dry and L-Wet regions, which suggests that dry-gets-drier hypothesis does not hold for dry grid cells delineated based on land-only PRCPTOT. In LECZ, the ensemble mean projected changes in PRCPTOT and RX1DAY were found to be 11% and 22%, respectively under RCP8.5. The implications of changes in precipitation extremes in LECZ should be carefully assessed as these regions are more vulnerable to flooding. Besides assessing changes in precipitation structure using four indices, this study also analyzed very rare events using the EVT framework. The average projected increase in 50-year return levels across land grids was found to be 14% and 22% for RCP4.5 and RCP8.5, respectively.

Large intermodel spread was noticed in the projections of all indices. The intermodel spread is particularly large when the analysis was conducted at seasonal scale. In general, the regional variability in projected changes was found to be more pronounced than the seasonal variability. However, some regions such as CSEA and PHIL exhibit strong annual cycle but dominated by large intermodel spread. As the fine resolution NEX-GDDP dataset is a result of statistical downscaling, the general limitations underlying statistical downscaling methods (e.g., stationarity assumption) will apply to the results presented in this study. Another caveat of this study is the bias correction in the NEX-GDDP dataset, which is carried out using the Global Meteorological Forcing Dataset of Sheffield et al. (2006). Further bias adjustment using regional datasets such

as APHRODITE (Yatagai et al., 2012) may improve the assessment of projected changes in precipitation at regional scales.

As risk is a function of hazard, exposure and vulnerability, the changes in precipitation structure need to be superposed on the changes in future exposure and vulnerability to assess their relative impacts on future riverine and coastal flood risk. With the recent progress in the availability of global flood hazard and exposure databases (e.g., Jongman et al., 2012; Jones and O'Neill, 2016), a few studies have assessed flood risk at global scale (e.g., Arnell and Gosling, 2016; Winsemius et al., 2016; Alfieri et al., 2017). Similar efforts at local scale using downscaled climate model projections and a more rigorous representation of changes in land use, land cover and population would help in better understanding of potential changes in flood risk and in framing future flood mitigation policies.

Acknowledgements

The authors acknowledge the support from the Singapore ETH Center Future Resilience Systems project. Climate scenarios used were from the NEX-GDDP dataset, prepared by the Climate Analytics Group and NASA Ames Research Center using the NASA Earth Exchange, and distributed by the NASA Center for Climate Simulation (NCCS). The authors also appreciate anonymous reviewers for their helpful comments.

References

- Ahmadalipour, A., H. Moradkhani and M. Svoboda, 2017: Centennial drought outlook over the CONUS using NASA-NEX downscaled climate ensemble. *Int J Climatol*, **37**, 2477–2491. doi:10.1002/joc.4859.
- Alexander, L. V. and J. M. Arblaster, 2009: Assessing trends in observed and modelled climate extremes over Australia in relation to future projections. *Int J Climatol*, **29**, 417–435. doi:10.1002/joc.1730.
- Alfieri, L., B. Bisselink, F. Dottori, G. Naumann, A. Roo, P. Salamon, K. Wyser and L. Feyen, 2017: Global projections of river flood risk in a warmer world. *Earth’s Future*, **5**, 171–182. doi:10.1002/2016EF000485.
- Arnell, N. W. and S. N. Gosling, 2016: The impacts of climate change on river flood risk at the global scale. *Climatic Change*, **134**, 387–401. doi:10.1007/s10584-014-1084-5.
- Bao, Y. and X. Wen, 2017: Projection of China’s near-and long-term climate in a new high-resolution daily downscaled dataset NEX-GDDP. *J Meteorol Res*, **31**, 236–249. doi:10.1007/s13351-017-6106-6.
- Budiyono, Y., J. Aerts, D. Tollenaar and P. Ward, 2015: River flood risk in jakarta under scenarios of future change. *Nat Hazards Earth Syst Sci Discuss*, **3**, 4435–4478. doi:10.5194/nhess-16-757-2016.
- Castillo, E., A. S. Hadi, N. Balakrishnan and J.-M. Sarabia, 2005: *Extreme Value and Related Models with Applications in Engineering and Science*. Wiley Hoboken, NJ.
- Chadwick, R., P. Good, G. Martin and D. P. Rowell, 2016: Large rainfall changes consistently projected over substantial areas of tropical land. *Nat Clim Change*, **6**, 177–181. doi:10.1038/nclimate2805.
- Chang, C., Z. Wang, J. McBride and C. Liu, 2005: Annual cycle of southeast asia-maritime continent rainfall and the asymmetric monsoon transition. *J Climate*, **18**, 287–301.

- Chen, H.-P., J.-Q. Sun and H.-X. Li, 2017: Future changes in precipitation extremes over china using the NEX-GDDP high-resolution daily downscaled data-set. *Atmos Ocean Sci Lett*, **10**, 403–410. doi:10.1080/16742834.2017.1367625.
- Chotamonsak, C., E. P. Salathé, J. Kreasuwan, S. Chantara and K. Siriwitayakorn, 2011: Projected climate change over southeast asia simulated using a WRF regional climate model. *Atmos Sci Lett*, **12**, 213–219. doi:10.1002/asl.313.
- Chun, J. A., S. Li, Q. Wang, W.-S. Lee, E.-J. Lee, N. Horstmann, H. Park, T. Veasna, L. Vandy, K. Pros and S. Vang, 2016: Assessing rice productivity and adaptation strategies for southeast asia under climate change through multi-scale crop modeling. *Agricul Syst*, **143**, 14–21. doi:10.1016/j.agry.2015.12.001.
- Coles, S., 2001: *An Introduction to Statistical Modeling of Extreme Values*. Springer.
- Daksiya, V., P. Mandapaka and E. Y. Lo, 2017: A comparative frequency analysis of maximum daily rainfall for a SE Asian region under current and future climate conditions. *Adv Meteorol*, **2017**. doi:10.1155/2017/2620798.
- Donat, M. G., A. L. Lowry, L. V. Alexander, P. A. OGorman and N. Maher, 2016: More extreme precipitation in the world’s dry and wet regions. *Nat Clim Change*, **6**, 508–513. doi:10.1038/NCLIMATE2941.
- Field, C. B., V. Barros, T. F. Stocker, Q. Dahe, D. J. David, E. L. Kristie and M. D. Michael, 2012: *Managing the Risks of Extreme Events and Disasters to Advance Climate Change Adaptation: Special Report of the Intergovernmental Panel on Climate Change*. Cambridge University Press, Cambridge, UK.
- Fischer, E. M., U. Beyerle and R. Knutti, 2013: Robust spatially aggregated projections of climate extremes. *Nat Clim Change*, **3**, 1033–1038. doi:10.1038/NCLIMATE2051.
- Food and Agricultural Organization, 2017: *FAOSTAT Database*.
- Gan, T. Y., 1998: Hydroclimatic trends and possible climatic warming in the Canadian Prairies. *Water Resour Res*, **34**, 3009–3015. doi:10.1029/98WR01265.

- Haraguchi, M. and U. Lall, 2015: Flood risks and impacts: A case study of Thailand's floods in 2011 and research questions for supply chain decision making. *Int J Disast Risk Re*, **14**, 256–272. doi:10.1016/j.ijdr.2014.09.005.
- Held, I. M. and B. J. Soden, 2006: Robust responses of the hydrological cycle to global warming. *J Climate*, **19**, 5686–5699. doi:10.1175/JCLI3990.1.
- Hess, A., H. Iyer and W. Malm, 2001: Linear trend analysis: a comparison of methods. *Atmos Environ*, **35**, 5211–5222. doi:10.1016/S1352-2310(01)00342-9.
- IPCC, 2014: *Climate Change 2014–Impacts, Adaptation and Vulnerability: Regional Aspects*. Cambridge University Press.
- Johnston, R., C. T. Hoanh, G. Lacombe, R. Lefroy, P. Pavelic and C. Fry, 2012: *Managing water in rainfed agriculture in the Greater Mekong Subregion. Final report prepared by IWMI for Swedish International Development Cooperation Agency (Sida)*. Colombo, Sri Lanka: International Water Management Institute (IWMI) Stockholm, Sweden: Swedish International Development Cooperation Agency.
- Jones, B. and B. O'Neill, 2016: Spatially explicit global population scenarios consistent with the Shared Socioeconomic Pathways. *Environ Res Lett*, **11**, 084003. doi:10.1088/1748-9326/11/8/084003.
- Jongman, B., P. J. Ward and J. C. Aerts, 2012: Global exposure to river and coastal flooding: Long term trends and changes. *Global Environ Change*, **22**, 823–835. doi:10.1016/j.gloenvcha.2012.07.004.
- Kao, S.-C. and A. R. Ganguly, 2011: Intensity, duration, and frequency of precipitation extremes under 21st-century warming scenarios. *J Geophys Res*, **116**, D16119. doi:10.1029/2010JD015529.
- Kendall, M., 1975: *Rank Correlation Methods*. Charles Griffin, London.
- Kharin, V. V., F. W. Zwiers, X. Zhang and G. C. Hegerl, 2007: Changes in temperature and precipitation extremes in the ipcc ensemble of global coupled model simulations. *J Climate*, **20**, 1419–1444. doi:10.1175/JCLI4066.1.

- Kharin, V. V., F. Zwiers, X. Zhang and M. Wehner, 2013: Changes in temperature and precipitation extremes in the CMIP5 ensemble. *Climatic change*, **119**, 345–357. doi:10.1007/s10584-013-0705-8.
- Kottegoda, N. T. and R. Rosso, 2008: *Applied statistics for civil and environmental engineers*. Blackwell Malden, MA.
- Lacombe, G., C. T. Hoanh and V. Smakhtin, 2012: Multi-year variability or unidirectional trends? Mapping long-term precipitation and temperature changes in continental Southeast Asia using PRECIS regional climate model. *Climatic Change*, **113**, 285–299. doi:10.1007/s10584-011-0359-3.
- Liu, C. and R. P. Allan, 2013: Observed and simulated precipitation responses in wet and dry regions 1850–2100. *Environ Res Lett*, **8**, 034002. doi:10.1088/1748-9326/8/3/034002.
- Mandapaka, P. V., X. Qin and E. Y. Lo, 2016: Seasonal and interannual variability of wet and dry spells over two urban regions in the western maritime continent. *J Hydrometeorol*, **17**, 1579–1600. doi:10.1175/JHM-D-15-0100.1.
- Mandapaka, P. V., X. Qin and E. Y. Lo, 2017: Analysis of spatial patterns of daily precipitation and wet spell extremes in Southeast Asia. *Int J Climatol*, **37**, 1161–1179. doi:10.1002/joc.5073.
- Masutomi, Y., K. Takahashi, H. Harasawa and Y. Matsuoka, 2009: Impact assessment of climate change on rice production in asia in comprehensive consideration of process/parameter uncertainty in general circulation models. *Agr, Ecosyst & Environ*, **131**, 281–291. doi:10.1016/j.agee.2009.02.004.
- Maurer, E. P., N. Roby, I. T. Stewart-Frey and C. M. Bacon, 2017: Projected twenty-first-century changes in the central american mid-summer drought using statistically downscaled climate projections. *Reg Environ Change*, **17**, 2421–2432. doi:10.1007/s10113-017-1177-6.
- McCuen, R., 2002: *Modeling hydrologic change: statistical methods*. CRC press, Boca Raton, FL.
- O’Gorman, P. A. and T. Schneider, 2009: The physical basis for increases in precipitation extremes in simulations of 21st-century climate change. *P Natl Acad Sci USA*, **106**, 14773–14777. doi:10.1073/pnas.0907610106.

- Pall, P., M. Allen and D. A. Stone, 2007: Testing the Clausius–Clapeyron constraint on changes in extreme precipitation under CO₂ warming. *Clim Dynam*, **28**, 351–363. doi:10.1007/s00382-006-0180-2.
- Pfahl, S., P. OGorman and E. Fischer, 2017: Understanding the regional pattern of projected future changes in extreme precipitation. *Nat Clim Change*, **7**, 423–427. doi:10.1038/NCLIMATE3287.
- Promchote, P., S. Y. Simon Wang and P. G. Johnson, 2016: The 2011 great flood in Thailand: Climate diagnostics and implications from climate change. *J Climate*, **29**, 367–379. doi:10.1175/JCLI-D-15-0310.1.
- Sen, P., 1968: Estimates of the regression coefficient based on Kendall’s tau. *J. Amer. Stat. Assoc.*, **63**, 1379–1389.
- Sheffield, J., G. Goteti and E. F. Wood, 2006: Development of a 50-year high-resolution global dataset of meteorological forcings for land surface modeling. *J Climate*, **19**, 3088–3111. doi:10.1175/JCLI3790.1.
- Sillmann, J., V. Kharin, F. Zwiers, X. Zhang and D. Bronaugh, 2013: Climate extremes indices in the CMIP5 multimodel ensemble: Part 2. future climate projections. *J Geophys Res - Atmos*, **118**, 2473–2493. doi:10.1002/jgrd.50188.
- Tan, M. L., A. L. Ibrahim, Z. Yusop, V. P. Chua and N. W. Chan, 2017: Climate change impacts under CMIP5 RCP scenarios on water resources of the Kelantan river basin, Malaysia. *Atmos Res*, **189**, 1–10. doi:10.1016/j.atmosres.2017.01.008.
- Taylor, K. E., R. J. Stouffer and G. A. Meehl, 2012: An overview of CMIP5 and the experiment design. *Bulletin of the American Meteorological Society*, **93**, 485–498. doi:10.1175/BAMS-D-11-00094.1.
- Thrasher, B. and R. Nemani, 2015: NASA earth exchange global daily downscaled projections (NEX-GDDP).
- Thrasher, B., E. P. Maurer, C. McKellar and P. Duffy, 2012: Bias correcting climate model simulated daily temperature extremes with quantile mapping. *Hydrol Earth Syst Sci*, **16**, 3309–3314. doi:10.5194/hess-16-3309-2012.

- Toreti, A., P. Naveau, M. Zampieri, A. Schindler, E. Scoccimarro, E. Xoplaki, H. A. Dijkstra, S. Gualdi and J. Luterbacher, 2013: Projections of global changes in precipitation extremes from coupled model intercomparison project phase 5 models. *Geophysical Research Letters*, **40**, 4887–4892. doi:10.1002/grl.50940.
- UNPD, 2015: *World Population Prospects - Data Booklet: The 2015 Revision (ST/ESA/SER.A/377)*. United Nations Department of Economic and Social Affairs, Population Division, New York.
- Van Vuuren, D. P., J. Edmonds, M. Kainuma, K. Riahi, A. Thomson, K. Hibbard, G. C. Hurtt, T. Kram, V. Krey, J.-F. Lamarque and T. Masui, 2011: The representative concentration pathways: an overview. *Climatic change*, **109**, 5. doi:10.1007/s10584-011-0148-z.
- Villarini, G., J. A. Smith, M. L. Baeck, R. Vitolo, D. B. Stephenson and W. F. Krajewski, 2011: On the frequency of heavy rainfall for the midwest of the United States. *J Hydrol*, **400**, 103–120. doi:10.1016/j.jhydrol.2011.01.027.
- Westra, S., L. V. Alexander and F. W. Zwiers, 2013: Global increasing trends in annual maximum daily precipitation. *J Climate*, **26**, 3904–3918. doi:10.1175/JCLI-D-12-00502.1.
- Winsemius, H. C., J. Aerts, L. P. van Beek, M. F. Bierkens, A. Bouwman, B. Jongman, J. C. Kwadijk, W. Ligtoet, P. L. Lucas, D. P. van Vuuren and P. J. Ward, 2016: Global drivers of future river flood risk. *Nat Clim Change*, **6**, 381–385. doi:10.1038/NCLIMATE2893.
- Wood, A. W., L. R. Leung, V. Sridhar and D. Lettenmaier, 2004: Hydrologic implications of dynamical and statistical approaches to downscaling climate model outputs. *Climatic change*, **62**, 189–216.
- World Bank, 2012: *Thai Flood 2011: Overview*. The World Bank, Bangkok, Thailand.
- World Bank, 2017: *World Development Indicators*. The World Bank, Washington, DC. <http://wdi.worldbank.org/table/4.2>, Accessed 5 November 2017.
- Yatagai, A., K. Kamiguchi, O. Arakawa, A. Hamada, N. Yasutomi and A. Kitoh, 2012: APHRODITE: Constructing a long-term daily gridded precipitation dataset for Asia based on a dense network of rain gauges. *Bull Amer Meteorol Soc*, **93**, 1401–1415. doi:10.1175/BAMS-D-11-00122.1.

- 583 Yue, S., P. Pilon and G. Cavadas, 2002: Power of the Mann–Kendall and Spearman’s
584 rho tests for detecting monotonic trends in hydrological series. *J Hydrol*, **259**, 254–271.
585 doi:10.1016/S0022-1694(01)00594-7.
- 586 Zhang, X., L. Alexander, G. C. Hegerl, P. Jones, A. K. Tank, T. C. Peterson, B. Trewin and
587 F. W. Zwiers, 2011: Indices for monitoring changes in extremes based on daily temperature
588 and precipitation data. *Wiley Interdisciplinary Reviews: Climate Change*, **2**, 851–870.

Table 1: List of indices employed to characterize precipitation structure

Indicator	Description	Units
PRCPTOT	Total wet day precipitation amount in a year or a season	mm
R10	Number of days with precipitation ≥ 10 mm d ⁻¹	days
R95P	Total precipitation from days with rainfall ≥ 95 th percentile	mm
RX1DAY	Annual or seasonal maximum daily precipitation	mm day ⁻¹

Table 2: List of regional masks and their fractional land coverage

Mask	Description	Land coverage (%)
CSEA	Continental Southeast Asia	27.3
SRMP	Sumatra and Malay Peninsula	14.9
JAVA	Java and nearby islands	6.5
BORS	Borneo and Sulawesi islands	20.6
PHIL	Philippines archipelago	8.9
NGUI	New Guinea	18.1
L-Dry	Dry (bottom 25 percentile precipitation) grid cells	25.0
L-Wet	Wet (top 25 percentile precipitation) grid cells	25.0
LECZ	Low elevation coastal zones	23.5

List of Figures

589	1	(a) Topography of the study region, (b) six geographical masks: continental southeast Asia (CSEA), Sumatra and Malay Peninsula (SRMP), JAVA, Borneo and Sulawesi islands (BORS), Philippines (PHIL), and New Guinea (NGUI), and (c) the model count for wet and dry grid cells. The wet and dry cells in (c) are derived based on top and bottom quartiles of the base period (1970-1999) PRCPTOT for each model.	27
596	2	Time series of four precipitation indices averaged over each region (CSEA, SRMP, JAVA, BORS, PHIL and NGUI). The solid thick lines represent ensemble mean and the shaded regions denote ± 1 standard deviation from 20 models.	28
597			
598			
599			
600	3	Same as Figure 2 but for L-dry, L-wet, and LECZ regions.	29
601	4	Maps showing spatial distribution of decadal trends (estimated using Sen's regression) in (top) PRCPTOT and (bottom) RX1DAY, for (left) RCP 4.5 and (right) RCP 8.5. Stippling indicates trends that are statistically significant at 5%.	30
602			
603			
604			
605	5	Maps showing spatial distribution of centennial changes (i.e. 2070-2099 vs 1970-1999) in (top) PRCPTOT and (bottom) RX1DAY, for (left) RCP 4.5 and (right) RCP 8.5. Stippling indicates that at least 15 models agree with the sign of ensemble mean change.	31
606			
607			
608			
609	6	Changes in precipitation indices averaged over nine regional masks (see Table 2) for the time period 2070-2099 relative to the 1970-1999 period. The vertical bars represent intermodel spread in the form of ensemble mean ± 1 standard deviation, and the shading indicates both intermodel spread and spatial variability. The dashed blue and red lines represent ensemble average across all land grid cells for RCP4.5 and RCP8.5.	32
610			
611			
612			
613			
614			
615	7	Changes in 50-year precipitation return level averaged over nine regional masks for the time period 2070-2099 relative to the 1970-1999 period. The vertical bars represent intermodel spread in the form of ensemble mean ± 1 standard deviation.	33
616			
617			
618			
619	8	Changes in precipitation indices averaged over nine regional masks for the time period 2070-2099 relative to the 1970-1999 period for different seasons. The vertical bars represent intermodel spread in the form of ensemble mean ± 1 standard deviation. The dashed line represents ensemble average across all land grid cells for RCP8.5.	34
620			
621			
622			
623			

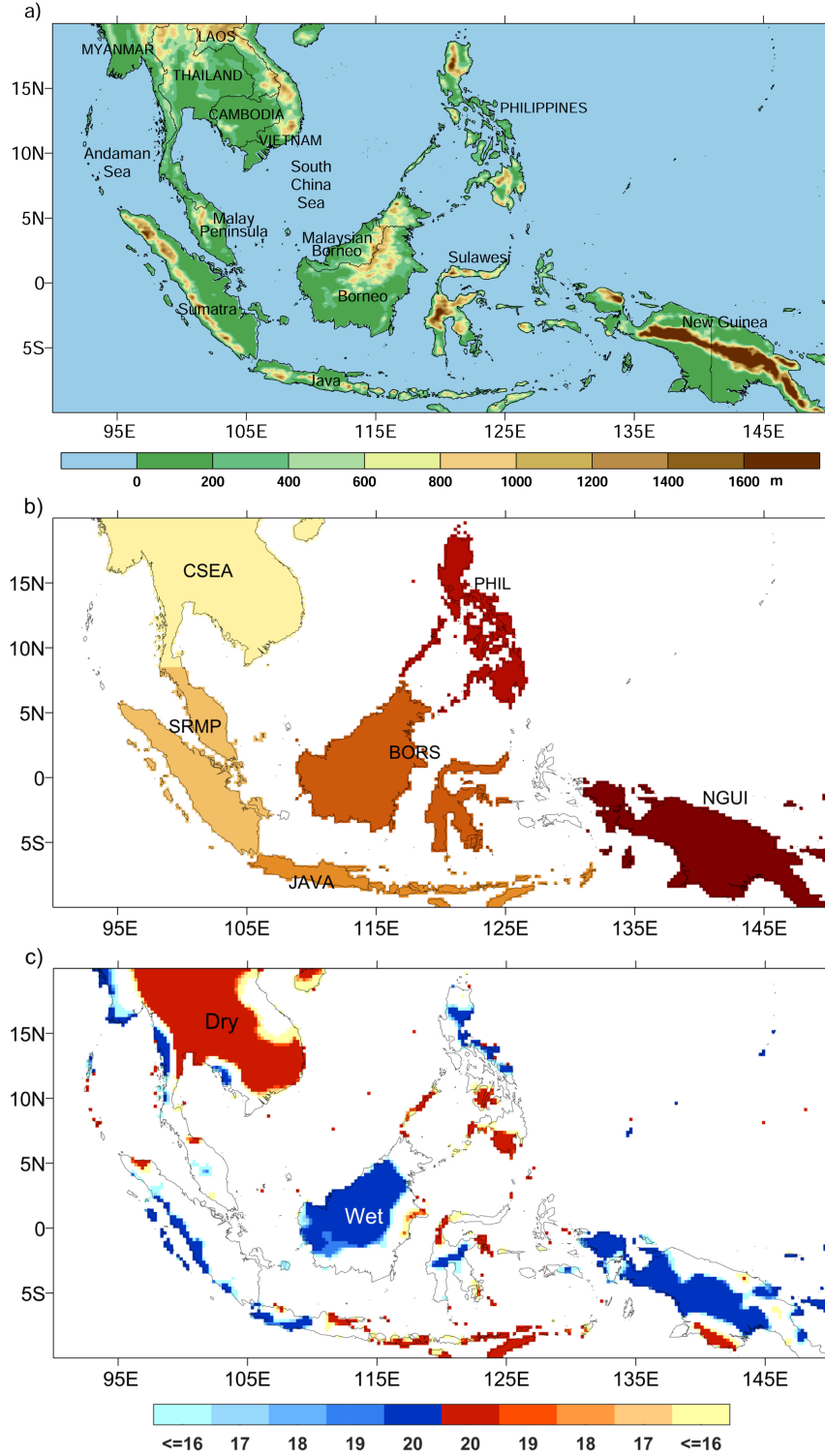


Figure 1: (a) Topography of the study region, (b) six geographical masks: continental south-east Asia (CSEA), Sumatra and Malay Peninsula (SRMP), JAVA, Borneo and Sulawesi islands (BORS), Philippines (PHIL), and New Guinea (NGUI), and (c) the model count for wet and dry grid cells. The wet and dry cells in (c) are derived based on top and bottom quartiles of the base period (1970-1999) PRCPTOT for each model.

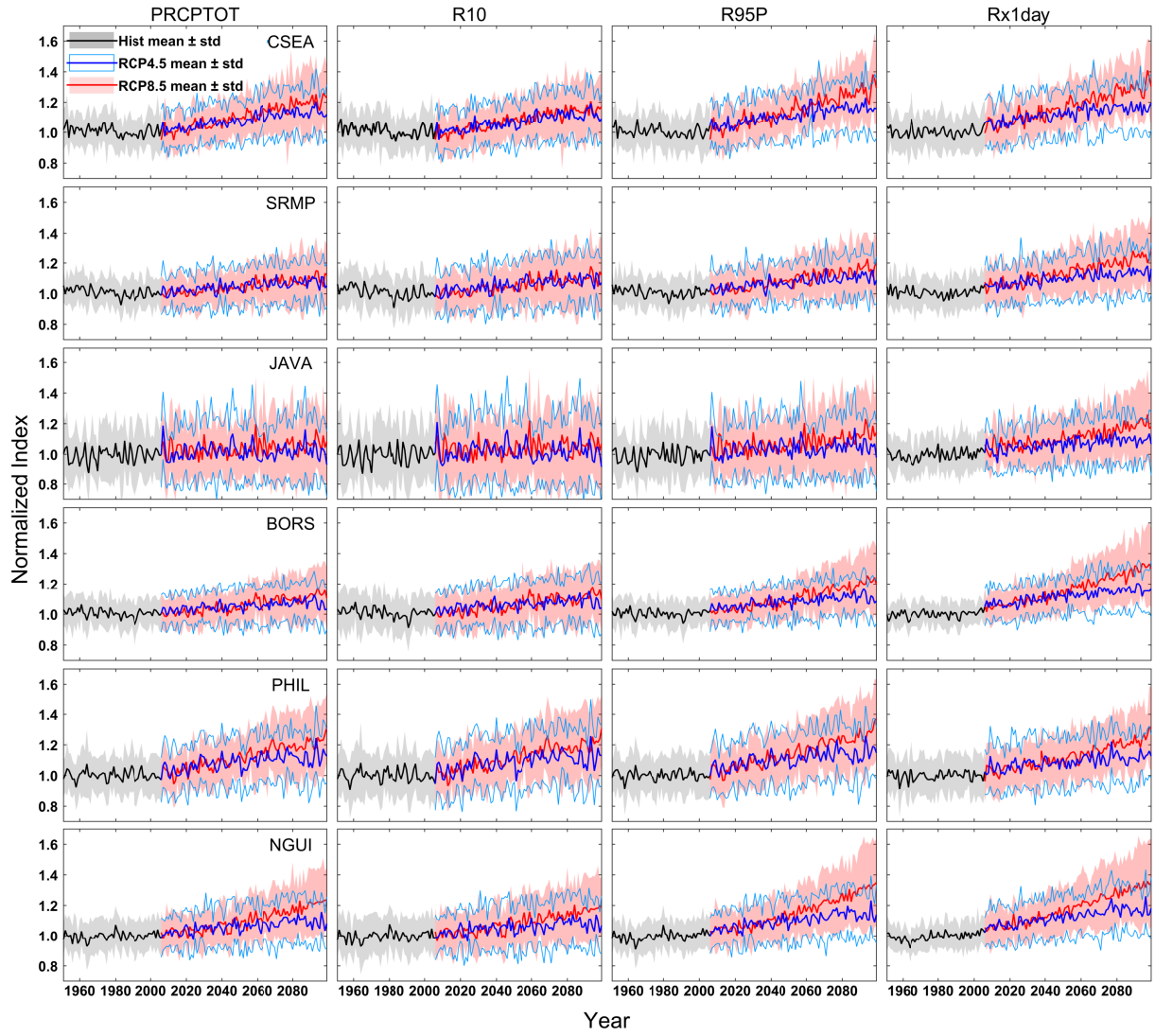


Figure 2: Time series of four precipitation indices averaged over each region (CSEA, SRMP, JAVA, BORS, PHIL and NGUI). The solid thick lines represent ensemble mean and the shaded regions denote ± 1 standard deviation from 20 models.

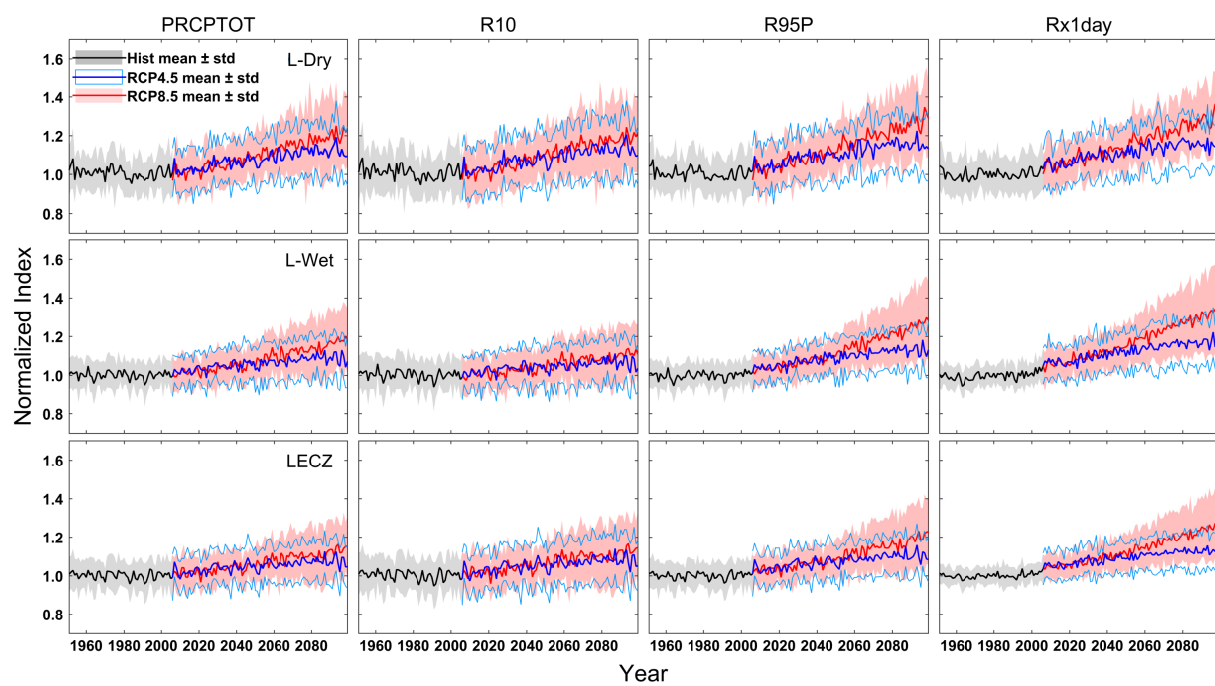


Figure 3: Same as Figure 2 but for L-dry, L-wet, and LECZ regions.

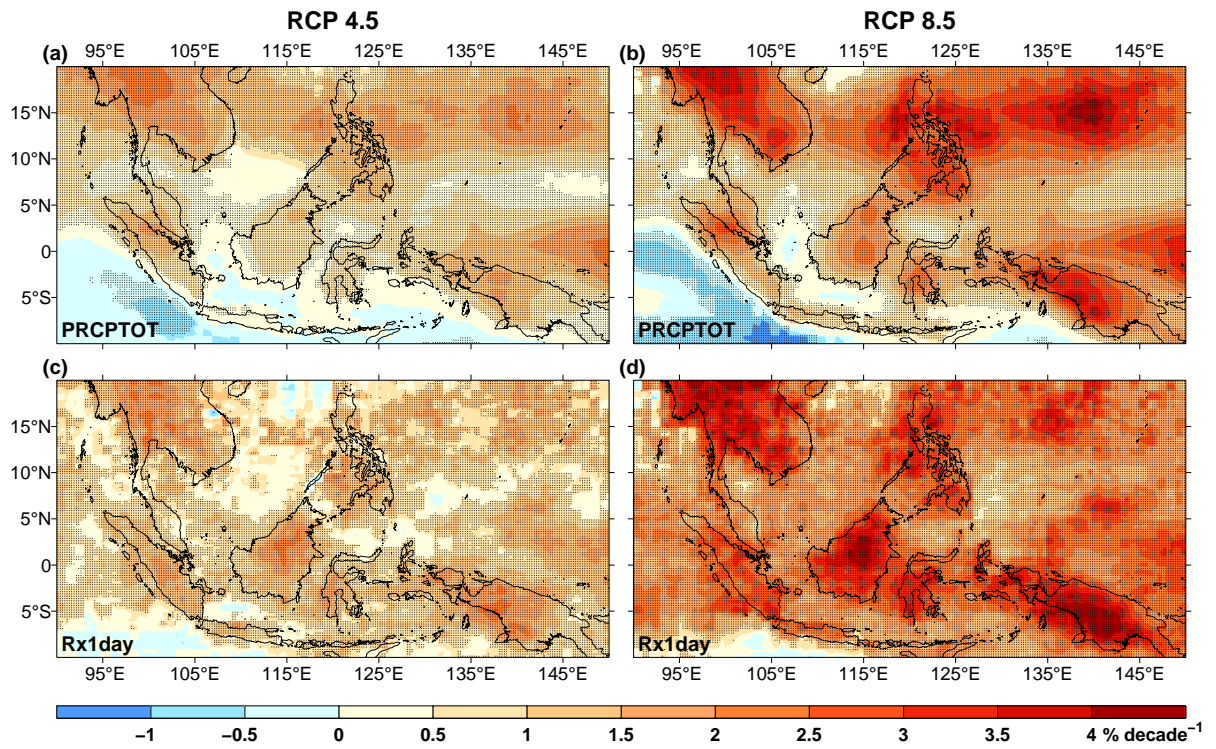


Figure 4: Maps showing spatial distribution of decadal trends (estimated using Sen's regression) in (top) PRCPTOT and (bottom) RX1DAY, for (left) RCP 4.5 and (right) RCP 8.5. Stippling indicates trends that are statistically significant at 5%.

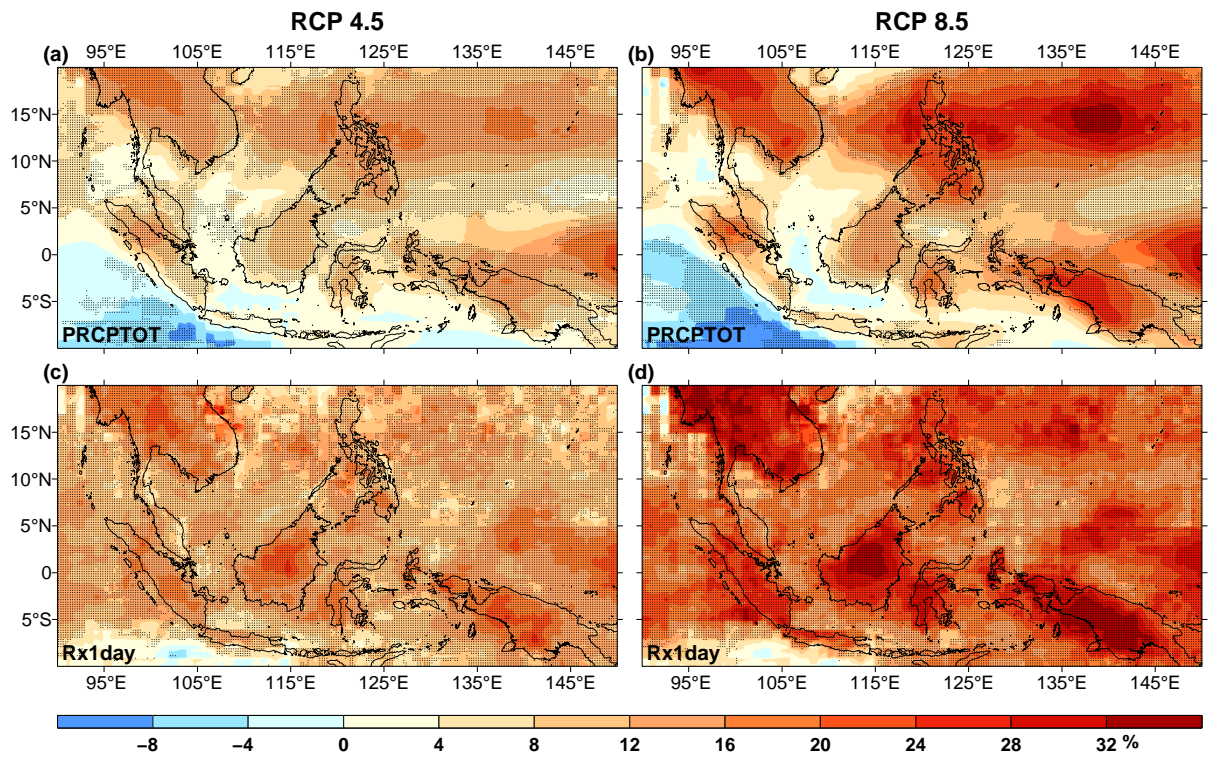


Figure 5: Maps showing spatial distribution of centennial changes (i.e. 2070-2099 vs 1970-1999) in (top) PRCPTOT and (bottom) RX1DAY, for (left) RCP 4.5 and (right) RCP 8.5. Stippling indicates that at least 15 models agree with the sign of ensemble mean change.

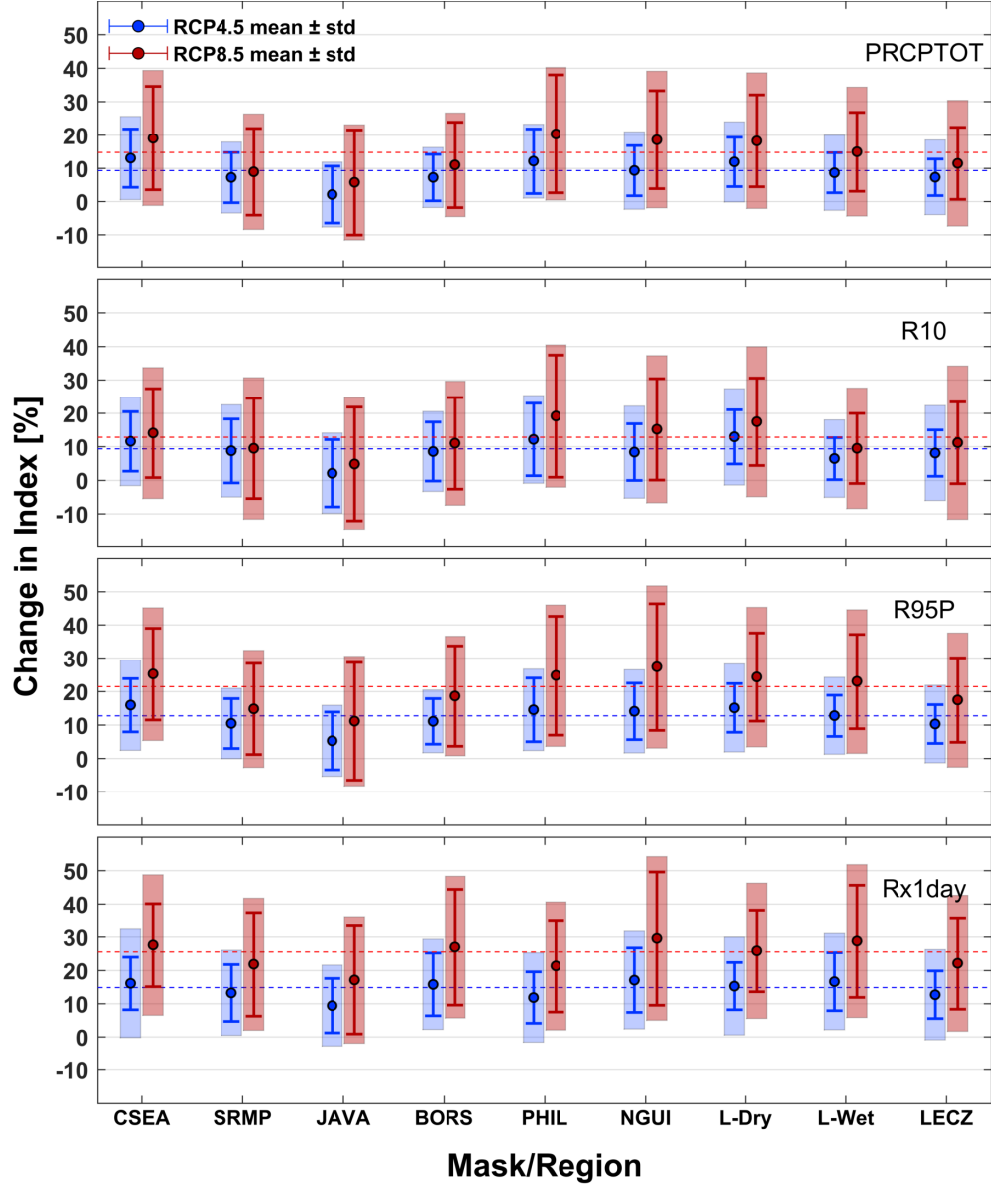


Figure 6: Changes in precipitation indices averaged over nine regional masks (see Table 2) for the time period 2070-2099 relative to the 1970-1999 period. The vertical bars represent intermodel spread in the form of ensemble mean ± 1 standard deviation, and the shading indicates both intermodel spread and spatial variability. The dashed blue and red lines represent ensemble average across all land grid cells for RCP4.5 and RCP8.5.

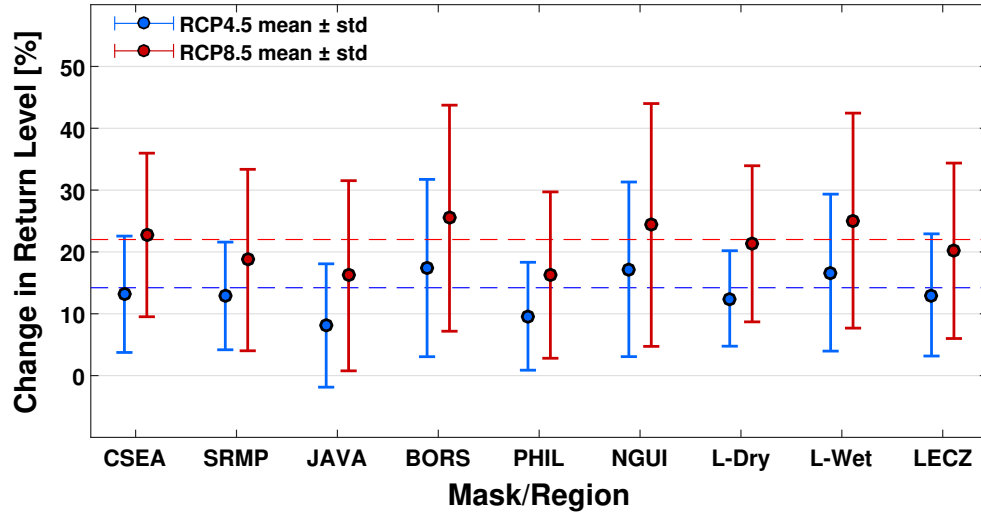


Figure 7: Changes in 50-year precipitation return level averaged over nine regional masks for the time period 2070-2099 relative to the 1970-1999 period. The vertical bars represent intermodel spread in the form of ensemble mean ± 1 standard deviation.

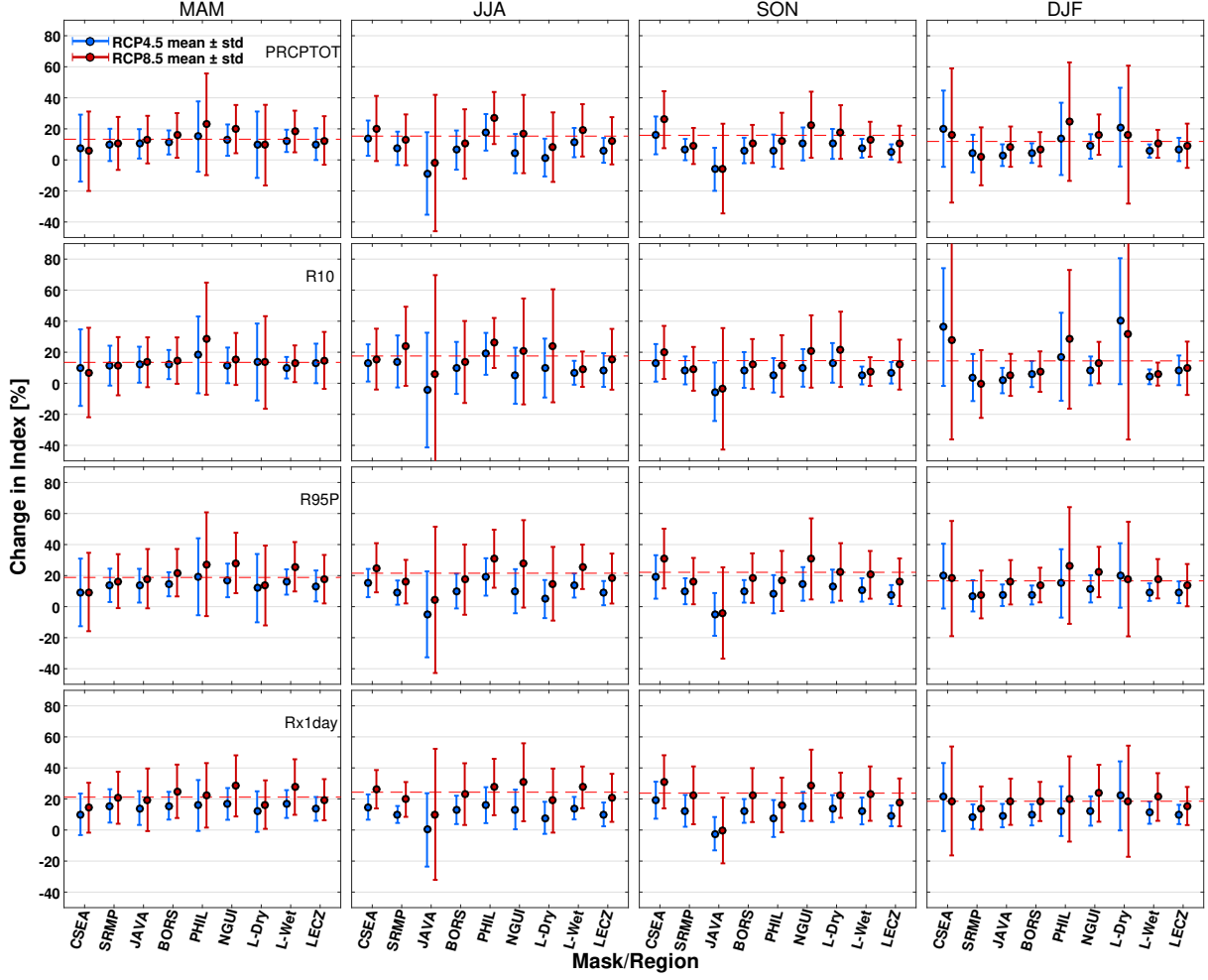


Figure 8: Changes in precipitation indices averaged over nine regional masks for the time period 2070-2099 relative to the 1970-1999 period for different seasons. The vertical bars represent intermodel spread in the form of ensemble mean ± 1 standard deviation. The dashed line represents ensemble average across all land grid cells for RCP8.5.